Entanglement of microwave-optical modes in a strongly coupled electro-optomechanical system

Changchun Zhong , 1,2,* Xu Han, 3,4 Hong X. Tang, 2,4 and Liang Jiang , 1,2,†

1 Pritzker School of Molecular Engineering, University of Chicago, Chicago, Illinois 60637, USA

2 Yale Quantum Institute, Yale University, New Haven, Connecticut 06520, USA

3 Center for Nanoscale Materials, Argonne National Laboratory, Argonne, Illinois 60439, USA

4 Department of Electrical Engineering, Yale University, New Haven, Connecticut 06520, USA

(Received 21 January 2020; accepted 9 March 2020; published 26 March 2020)

Quantum transduction between microwaves and optics can be realized by quantum teleportation if given reliable microwave-optical entanglement, namely, entanglement-based quantum transduction. To realize this protocol, an entangled source with a high fidelity between the two frequencies is necessary. In this paper, we study microwave and optical entanglement generation based on a generic cavity electro-optomechanical system in the strong coupling regime. Splittings are shown in the microwave and optical output spectra and the frequency entanglement between the two modes is quantified. We show that entanglement can be straightforwardly encoded in the frequency-bin degree of freedom and propose a feasible experiment to verify entangled photon pairs. The experimental implementation is systematically analyzed, and the preferable parameter regime for entanglement verification is identified. An inequality is given as a criterion for good entanglement verification with analysis of practical imperfections.

DOI: 10.1103/PhysRevA.101.032345

I. INTRODUCTION

Building a distributed quantum architecture, where distant quantum circuits are connected through low-loss optical communication channels, is a long-pursued goal in the quantum computation community [1–4]. To realize this goal, an essential part is to coherently transfer quantum states between the optical channels and the quantum circuits, which in general are in quite different frequency ranges, e.g., optical telecom photons at \sim 200 THz and superconducting circuits at ~10-GHz microwave frequencies. However, a superconducting qubit does not directly interact with optical photons; a high-fidelity quantum transducer is thus urgently needed to interface microwave and optical (M-O) photons in a coherent way. The development of an efficient transducer will not only expand the superconducting quantum network but also connect superconducting qubits with different quantum modules [5-11].

Quantum state transduction can be realized by either direct quantum transduction (DT), which linearly converts photons between different frequencies [12–30], or entanglement-based transduction (ET), which first generates entangled photon pairs (or continuous bosonic modes) with different frequencies, then completes the transduction with quantum teleportation [31–33]. Recently, theoretical proposals given an imperfect DT transducer show the possibility of achieving state transduction by choosing squeezed ancillary input and performing feedforward [34–36]. Experimentally, the feedforward scheme has already shown a great enhancement of the transducer performance [37]. Despite this encouraging

progress, an efficient quantum-enabled M-O transducer remains to be demonstrated, mainly due to the demanding requirements of a high conversion efficiency threshold and low added thermal noise. In contrast, ET does not require the threshold conversion efficiency because of the introduction of classical communication channels and, thus, is more compatible with the current technological developments [31,38,39].

A major step in ET is to demonstrate useful entanglement between microwave and optical photon pairs (or continuous modes). In Ref. [31], M-O time-bin entanglement generation and detection based on a generic cavity electro-optomechanical system have been investigated in the weak coupling regime, where a wide range of feasible parameters in this regime can be used to demonstrate M-O entanglement. Especially, the verification could tolerate a certain amount of thermal noise, which is compatible with recent experiments: the design of a mechanical mode in contact with a 1 K thermal bath (to enhance the power handling capability [31,40]), which is shown to be below the noise threshold.

In this paper, we propose an M-O frequency-bin entanglement generation and detection scheme based on a generic electro-optomechanical system in the strong coupling regime. For analysis, we consider a cavity piezo-optomechanical system [39,41]. By exploiting the strong-coupling-induced hybridization between the microwave and the mechanical modes, we discuss frequency-entangled M-O states under an optomechanical parametric down-conversion process. The entanglement is characterized by calculating the entanglement of formation (E_F) of the output modes. Furthermore, we define an entanglement rate (E_R) to quantify the overall efficiency of entanglement generation, which is shown to reach a maximum when the system approaches the exceptional point—a recently well-studied concept in non-Hermitian quantum mechanics [42]. To observe the

 $^{^*}zhong.changchun@uchicago.edu\\$

[†]liang.jiang@uchicago.edu

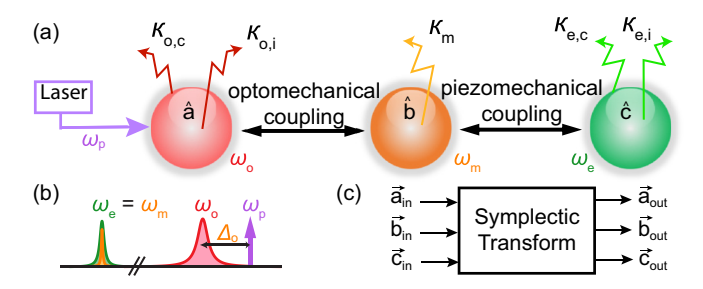


FIG. 1. (a) Schematic of a piezo-optomechanical system with a blue-detuned laser drive. (b) The frequency landscape for the microwave, mechanical, and optical resonators and the pump laser. (c) The Gaussian unitary transformation connecting input and output mode operators. Take $\vec{a}_{in} = (\hat{a}_{in,c}, \hat{a}_{in,i})$, and other vectors are similarly defined.

entanglement experimentally, we propose a heralded scheme that detects entangled photon pairs in the frequency-bin degree of freedom. We map out the preferable parameter regime satisfying the entanglement criteria (Bell inequality violation or Bell state fidelity). Moreover, the entangled M-O mode correlation function and coincidence count rate of output photons are theoretically estimated. A criterion for good entanglement verification taking into account dark counts, transmission loss, and detection inefficiency is derived in the end. The entanglement analysis and proposed detection scheme could be generalized to quantum transducers based on different physical platforms, thus providing a useful framework for analyzing M-O entanglement in the strong coupling regime.

II. PIEZO-OPTOMECHANICAL SYSTEM WITH A BLUE-DETUNED DRIVE

Without losing generality, our discussion is based on a piezo-optomechanical system with a blue-detuned laser pump, as shown schematically in Fig. 1; a mechanical resonator is, on one side, parametrically coupled to an optical cavity by radiation pressure and, on the other side, linearly coupled to a microwave resonator through piezoelectric force. Denoting \hat{a} , \hat{b} , and \hat{c} the optical, mechanical, and microwave mode operators, respectively, and ω_0 , ω_m , and ω_e the corresponding resonant frequencies, we can write the linearized Hamiltonian of the system with the rotating wave approximation [20,31]:

$$\hat{H} = -\hbar \Delta_{o} \hat{a}^{\dagger} \hat{a} + \hbar \omega_{m} b^{\dagger} \hat{b} + \hbar \omega_{e} \hat{c}^{\dagger} \hat{c} - \hbar g_{om} (\hat{a}^{\dagger} \hat{b}^{\dagger} + \hat{a} \hat{b}) - \hbar g_{em} (\hat{b}^{\dagger} \hat{c} + \hat{b} \hat{c}^{\dagger}).$$
(1)

It is noteworthy that the above Hamiltonian is general for different physical platforms, and thus the theory framework developed below is applicable to various systems [14,19,20,39]. For the piezo-optomechanical system, $g_{\rm em}$ is the piezoelectrical coupling. $g_{\rm om} := \sqrt{\bar{n}_{\rm o}} g_{{\rm om},0}$ is the optomechanical coupling strength, where $g_{{\rm om},0}$ denotes the single-photon coupling. In experiments, the optical cavity will be pumped on the blue side band by a laser with a frequency $\omega_{\rm p} = \omega_{\rm o} + \Delta_{\rm o}$ and is populated with $\bar{n}_{\rm o}$ photons on average, which can further enhance the optomechanical coupling. In the discussion that follows, we take the resonance condition $\Delta_{\rm o} = \omega_{\rm m,e}$.

The above system is able to generate entanglement between microwave and optical modes, which is realized intuitively by first entangling the optical and mechanical modes with a two-mode squeezing interaction; meanwhile the mechanical excitation is swapped to the microwave mode by the beam-splitter-type coupling. To analyze the complete dynamics of the system, we write the linearized Heisenberg-Langevin equations of motion for each mode,

$$\begin{split} \dot{\hat{a}}^{\dagger} &= \left(-i\Delta_{\rm o} - \frac{\kappa_{\rm o}}{2} \right) \hat{a}^{\dagger} - ig_{\rm om}\hat{b} + \sqrt{\kappa_{\rm o,c}} \hat{a}_{\rm in,c}^{\dagger} + \sqrt{\kappa_{\rm o,i}} \hat{a}_{\rm in,i}^{\dagger}, \\ \dot{\hat{b}} &= \left(-i\omega_{\rm m} - \frac{\kappa_{\rm m}}{2} \right) \hat{b} + ig_{\rm om}\hat{a}^{\dagger} + ig_{\rm em}\hat{c} + \sqrt{\kappa_{\rm m}} \hat{b}_{\rm in}, \\ \dot{\hat{c}} &= \left(-i\omega_{\rm e} - \frac{\kappa_{\rm e}}{2} \right) \hat{c} + ig_{\rm em}\hat{b} + \sqrt{\kappa_{\rm e,c}} \hat{c}_{\rm in,c} + \sqrt{\kappa_{\rm e,i}} \hat{c}_{\rm in,i}, \end{split}$$
 (2)

where we label the optical, mechanical, and microwave decay rates $\kappa_0 = \kappa_{o,c} + \kappa_{o,i}$, κ_m , and $\kappa_e = \kappa_{e,c} + \kappa_{e,i}$. The subscript "i" stands for the internal loss port, "c" for the coupling port, and "in" for the input noise operator. Equations (2) admit a set of Hermitian conjugate equations, having essentially the same physics. All input noise operators satisfy [44]

$$[\hat{o}_{\text{in}}^{\dagger}(t), \hat{o}_{\text{in}}(t')] = \bar{n}\delta(t - t'),$$

$$[\hat{o}_{\text{in}}(t), \hat{o}_{\text{in}}^{\dagger}(t')] = (\bar{n} + 1)\delta(t - t').$$
(3)

To comply with the experimental condition, we assume that the mechanical resonator and the microwave internal port couple to a thermal bath $\bar{n} = \bar{n}_{\text{ba}} = (e^{\hbar \omega_{\text{mic}}/k_{\text{B}}T} - 1)^{-1}$, while the optical resonator and the microwave coupling port are subjected to purely vacuum fluctuations $\bar{n} = 0$. In experiments, the microwave coupling is in contact with a millikelvin cold bath, which could radiatively cool the system close to the ground state. This radiative cooling was recently demonstrated in superconducting resonators [40] and is significant in observing M-O entanglement in our design.

The output modes can be obtained by combining the coupled Eqs. (2) with the input-output formalism (taking the optical mode, for example),

$$\hat{a}_{\text{out,c}} = \sqrt{\kappa_{\text{o,c}}} \hat{a} - \hat{a}_{\text{in,c}}, \quad \hat{a}_{\text{out,i}} = \sqrt{\kappa_{\text{o,i}}} \hat{a} - \hat{a}_{\text{in,i}}, \quad (4)$$

where the subscript "out" denotes the output mode. Thus, the system defines a Gaussian unitary channel which is captured by a symplectic transform $\mathbf{x}_{\text{out}} = \mathbf{S}\mathbf{x}_{\text{in}}$ [45,46], where \mathbf{S} is the symplectic transformation matrix. \mathbf{x}_{in} and the vectors \mathbf{x}_{out} collect all the input and output quadratures. If we label the M-O output state quadratures $\mathbf{x} = (\hat{x}_{\text{o}}, \hat{p}_{\text{o}}, \hat{x}_{\text{e}}, \hat{p}_{\text{e}})$, a covariance matrix $\mathbf{V}_{\text{oe}}^{\text{out}}$ with the elements defined by $V_{ij} = \frac{1}{2} \langle \{\hat{x}_i - \langle \hat{x}_i \rangle, \hat{x}_j - \langle \hat{x}_j \rangle \} \rangle$ can be obtained, and it can be expressed in the standard form,

$$\mathbf{V}_{\text{oe}}^{\text{out}} = \begin{pmatrix} \mathbf{V}_{u} & \mathbf{V}_{w} \\ \mathbf{V}_{w} & \mathbf{V}_{v} \end{pmatrix}$$

$$= \begin{pmatrix} u(\omega) & 0 & -w(\omega) & 0 \\ 0 & u(\omega) & 0 & w(\omega) \\ -w(\omega) & 0 & v(\omega) & 0 \\ 0 & w(\omega) & 0 & v(\omega) \end{pmatrix}, \quad (5)$$

where V_u , V_v , and V_w are the corresponding two-dimensional matrix blocks. This matrix fully characterizes the output M-O

TABLE I. Parameters used in numerical evaluations in the text (unless specified otherwise). To comply with the experiment, we leave \mathcal{C}_{om} and $\kappa_{e,c}$ tunable, which can be realized by controlling the optical pump strength and the position of the microwave readout probe [43].

g _{em} (MHz)	κ _{e,i} (kHz)	κ _{o,i} (GHz)	$\kappa_{\mathrm{o,c}}$	κ _m (kHz)
$2\pi \times 2.0$	$2\pi \times 100$	$2\pi \times 0.24$	$\kappa_{\mathrm{o,i}}$	$2\pi \times 20$

Gaussian state, where the diagonal elements represent the corresponding output power spectrum densities and other elements indicate the quadrature correlations.

III. THE PIEZOMECHANICAL STRONG COUPLING REGIME

When the mode coupling rate is larger than the mode losses, the system is said to be in the strong coupling regime, where mode hybridization occurs. We show later that this enables us to conveniently encode entangled photon pairs in the frequency degree of freedom. Using the feasible parameters listed in Table I, we first numerically calculate the M-O output power spectrum densities with respect to the ratio $\mathcal{R} = \kappa_e/4g_{em}$, which measures how strongly ($\mathcal{R} < 1$) or weakly $(\mathcal{R} > 1)$ coupled the system is. [Strictly speaking, we should define $\mathcal{R} = (\kappa_{\rm e} - \kappa_{\rm m})/4g_{\rm em}$. We omitted $\kappa_{\rm m}$ since it is relatively small. Details are shown later.] As shown in Fig. 2, two peaks can be clearly resolved in both the optical and the microwave output spectra as the system approaches the piezomechanical strong coupling regime. Intuitively, the splitting of the microwave output mode is due to the hybridization between the microwave and the mechanical modes, while the splitting in the optical mode results from the energy conservation. This can be seen more rigorously from Eq. (2). To show this, we recast Eq. (2) into a more compact form in the microwave rotating frame (we use this frame in all later discussion),

$$\dot{\mathbf{a}} = \mathbf{M}\mathbf{a} + \mathbf{N}\mathbf{a}_{in},\tag{6}$$

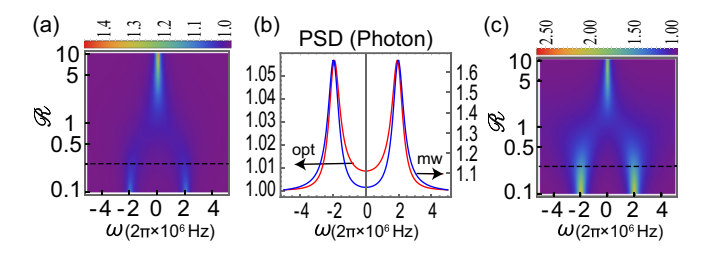


FIG. 2. Output power spectrum densities for (a) the optical mode and (c) the microwave mode, where mode splitting of $2g_{em}$ appears when the ratio $\mathcal{R}=\kappa_e/4g_{em}$ is decreased. The ratio $\mathcal{R}=1$ separates the weak and the strong coupling regimes. Dashed black lines in (a) and (c) correspond to the red (opt) and blue (mw) curves in (b) with the ratio $\mathcal{R}=0.2$. In these plots, parameters from Table I are used and $\bar{n}_{ba}=1$, $\mathcal{C}_{om}=1$.

where we group the operators into the vectors $\mathbf{a}_{in} = (\hat{a}_{in.c}^{\dagger}, \hat{a}_{in.i}^{\dagger}, \hat{b}_{in}, \hat{c}_{in.c}, \hat{c}_{in.i})^{T}, \mathbf{a} = (\hat{a}^{\dagger}, \hat{b}, \hat{c})^{T}$. The matrices

$$\mathbf{M} = \begin{pmatrix} -\frac{\kappa_{0}}{2} & -ig_{\text{om}} & 0\\ ig_{\text{om}} & -\frac{\kappa_{\text{m}}}{2} & ig_{\text{em}}\\ 0 & ig_{\text{em}} & -\frac{\kappa_{e}}{2} \end{pmatrix}, \tag{7}$$

$$\mathbf{N} = \begin{pmatrix} 0 & ig_{\text{em}} & -\frac{\kappa_e}{2} \end{pmatrix}$$

$$\mathbf{N} = \begin{pmatrix} \sqrt{\kappa_{\text{o,c}}} & \sqrt{\kappa_{\text{o,i}}} & 0 & 0 & 0\\ 0 & 0 & \sqrt{\kappa_{\text{m}}} & 0 & 0\\ 0 & 0 & 0 & \sqrt{\kappa_{\text{e,c}}} & \sqrt{\kappa_{\text{e,i}}} \end{pmatrix}.$$
(8)

The non-Hermitian dynamical matrix \mathbf{M} determines the normal modes. Taking the approximation $\kappa_{\rm o} \gg g_{\rm om}$ (a relatively lossy optical cavity in experiments), one finds the hybridized normal modes of the microwave and mechanical resonator with eigenvalues

$$\lambda_{B,C} = -\frac{\kappa_{\rm e} + \kappa_{\rm m}}{4} \mp \sqrt{-g_{\rm em}^2 + \left(\frac{\kappa_{\rm e} - \kappa_{\rm m}}{4}\right)^2}, \qquad (9)$$

where the subscripts B and C represent the two hybridized modes. When $g_{\rm em} > |\kappa_{\rm e} - \kappa_{\rm m}|/4$, a negative value of the square root is achieved, which corresponds to a mode splitting $2\sqrt{g_{\rm em}^2 - ((\kappa_{\rm e} - \kappa_{\rm m})/4)^2}$. When $g_{\rm em}$ dominates $g_{\rm em} \gg |\kappa_{\rm e} - \kappa_{\rm m}|4$, the mode splitting approaches $2g_{\rm em} \sim 2\pi \times 4$ MHz, which is exactly what we show in Fig. 2 in the strong coupling limit. In this limit, we can approximately define the two hybridized modes as [47]

$$\hat{B} = \frac{\sqrt{2}}{2}(\hat{b} + \hat{c}), \quad \hat{C} = \frac{\sqrt{2}}{2}(\hat{b} - \hat{c}),$$
 (10)

by which the Hamiltonian, Eq. (1), can be rewritten as

$$\hat{H} = -\hbar \Delta_{o} \hat{a}^{\dagger} \hat{a} + \hbar \omega_{B} \hat{B}^{\dagger} \hat{B} + \hbar \omega_{C} \hat{C}^{\dagger} \hat{C}$$

$$- \frac{\sqrt{2} \hbar g_{om}}{2} (\hat{a}^{\dagger} \hat{B}^{\dagger} + \hat{a} \hat{B}) - \frac{\sqrt{2} \hbar g_{om}}{2} (\hat{a}^{\dagger} \hat{C}^{\dagger} + \hat{a} \hat{C}), \quad (11)$$

where $\omega_{\rm B} = \omega_{\rm m} - g_{\rm em}$ and $\omega_{\rm C} = \omega_{\rm e} + g_{\rm em}$ are the new mode frequencies. Thus, we obtain two two-mode squeezing interactions between the optical mode and each of the hybridized modes, which could simultaneously generate entanglement between either modes \hat{a} and \hat{B} or modes \hat{a} and \hat{C} . It is noteworthy that the above approximation is not always true; in our calculation we choose experimentally compatible parameters with the optomechanical cooperativity $\mathcal{C}_{\text{om}} \equiv \frac{4g_{\text{om}}^2}{\kappa_0 \kappa_m} \sim 1$, indicating a good approximation. To be theoretically complete, when $g_{\rm em} < |\kappa_{\rm e} - \kappa_{\rm m}|/4$, a positive value is taken for the square root and the system is considered to be in the weak coupling regime. Especially, when $g_{\rm em} = |\kappa_{\rm e} - \kappa_{\rm m}|/4$, the eigenvalues as well as the eigenvectors coincide, which corresponds with the exceptional point well known in non-Hermitian quantum physics [42,48,49]. We thus define a ratio $\mathcal{R} = \kappa_{\rm e}/4g_{\rm em}$ to quantify how strongly ($\mathcal{R} < 1$) or weakly $(\mathcal{R} > 1)$ coupled the system is, as mentioned before, and $\mathcal{R} = 1$ corresponds to the exceptional point.

IV. CHARACTERIZATION OF THE OUTPUT M-O STATE ENTANGLEMENT

Ideally, in the strong coupling regime, a product of the twomode squeezed vacuum state can be obtained when analyzing the Hamiltonian, Eq. (11), written as

$$|\Psi\rangle_{\text{eo}} \simeq \sum_{n_{1}=0}^{\infty} \frac{r_{1}^{n_{1}}}{\sqrt{n_{1}!}} (\hat{a}_{1}^{\dagger})^{n_{1}} (\hat{B}^{\dagger})^{n_{1}} |\text{vac}\rangle$$

$$\otimes \sum_{n_{2}=0}^{\infty} \frac{r_{2}^{n_{2}}}{\sqrt{n_{2}!}} (\hat{a}_{2}^{\dagger})^{n_{2}} (\hat{C}^{\dagger})^{n_{2}} |\text{vac}\rangle, \qquad (12)$$

where we define \hat{a}_1 and \hat{a}_2 as the optical modes that match the frequencies of the hybridized modes \hat{B} and \hat{C} due to energy conservation. r_1 and r_2 are the effective squeezing factors, which are determined by the optical pump strength and the interaction time before the photons leak out of the cavity. Due to symmetry in our case, we have $r := r_1 = r_2$. For a weak laser pump, $r \ll 1$ and thus

$$|\Psi\rangle_{eq} \simeq |\text{vac}\rangle + r(\hat{a}_1^{\dagger}\hat{B}^{\dagger} + \hat{a}_2^{\dagger}\hat{C}^{\dagger})|\text{vac}\rangle + O(r^2).$$
 (13)

We see that a Bell state can be generated with probability $|r|^2$. When the state is coupled out of the cavity, neglecting higher-order terms in r and discarding the vacuum state (by postselection), we can get a standard Bell state encoded in the frequency-bin degree of freedom.

In reality, due to the dissipation and thermal fluctuation, the M-O state is generally a mixed Gaussian state. Thus we can only obtain a mixed two-mode Gaussian state, as indicated by the output covariance matrix, Eq. (5). In order to characterize the output state, we first use the entanglement of formation E_F to quantify its entanglement. For a given state, E_F is defined as the least average von Neumann entropy optimized over all possible pure state decompositions. For an output state given in the form of Eq. (5), E_F can be evaluated by the formula [50,51]

$$E_F(\omega) = \cosh^2 r_0 \, \log_2(\cosh^2 r_0) - \sinh^2 r_0 \, \log_2(\sinh^2 r_0),$$
(14)

where r_0 is the minimum amount of antisqueezing needed to disentangle the state and it is given by

$$r_0 = \frac{1}{4} \ln \left(\frac{\gamma - \sqrt{\gamma^2 - \beta_+ \beta_-}}{\beta_-} \right), \tag{15}$$

with

$$\gamma = 2\left(\det \mathbf{V}_{\text{oe}}^{\text{out}} + 1\right) - (u(\omega) - v(\omega))^{2},$$

$$\beta_{\pm} = \det \mathbf{V}_{u} + \det \mathbf{V}_{v} - 2\det \mathbf{V}_{w} + 2u(\omega)v(\omega) + 2w^{2}(\omega) \pm 4w(\omega)(u(\omega) + v(\omega)).$$
(16)

Using the feasible parameters listed in Table I, we estimate the squeezing r_0^2 to be of the order of 0.1, which corresponds to a 10% probability of generating a Bell state. Thus the higher order in Eq. (13) can be neglected due to this weak squeezing approximation. In general, the squeezing parameter r_0 is frequency dependent. For $\omega = 0$ and in the low thermal noise limit, it can be simplified to

$$r_0 = \frac{1}{2} \ln \frac{1 + (\sqrt{C_{\text{om}}} + \sqrt{C_{\text{em}}})^2}{1 + (\sqrt{C_{\text{om}}} - \sqrt{C_{\text{em}}})^2},$$
 (17)

where $\mathcal{C}_{em} \equiv \frac{4g_{em}^2}{\kappa_e \kappa_m}$ is the electromechanical cooperativity. As expected, a larger squeezing can be obtained when

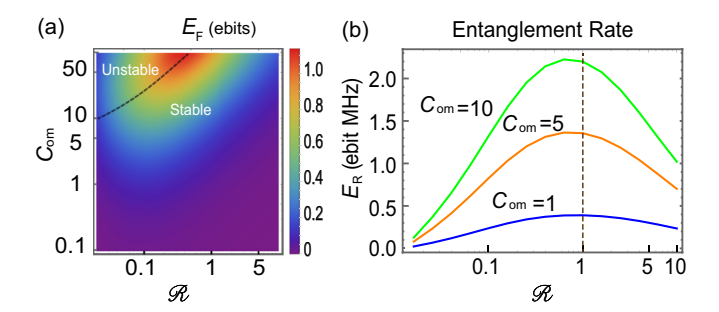


FIG. 3. (a) $E_{\rm F}(\omega)$ with $\omega=g_{\rm em}=2\pi\times 2$ MHz (in the rotating frame) in terms of $\mathcal{C}_{\rm om}$ and the ratio $\mathscr{R}=\kappa_{\rm e}/4g_{\rm em}$. The dashed line separates the stable and unstable parameter regimes. (b) Entanglement rate for varied $\mathcal{C}_{\rm om}$. The dashed vertical line is given by $\mathscr{R}=1$, which separates the weak and the strong coupling regimes. In these plots, parameters in Table I are used and $\bar{n}_{\rm ba}=1$.

 $\mathcal{C}_{\text{om}} \sim \mathcal{C}_{\text{em}}$, which corresponds to the strong parametric down-conversion regime. By fixing the output frequency $\omega = 2\pi \times 2$ MHz [52], we calculate E_F by scanning the ratio $\mathcal{R} = \kappa_e/4g_{\text{em}}$ ($g_{\text{em}} = 2\pi \times 2$ MHz). As shown in Fig. 3(a), entanglement is generated for any nonzero squeezing $r_0 > 0$ and reaches a maximum along the dashed line, where the system is approaching the strong parametric down-conversion regime. Interestingly, this dashed line marks the boundary between system stability and system instability. By numerically checking the stability condition of Eq. (6) [53–55], the system is shown to be unstable as \mathcal{C}_{om} increases, shown by the area above the dashed line in Fig. 3(a). The reason is that when the blue-detuned laser drive becomes too strong, the optomechanical parametric gain will be too large and cause instability.

The quantity $E_F(\omega)$ measures the amount of entanglement in the output state for a given frequency. In practice, it is also important to check the entanglement within a certain bandwidth. Due to energy conservation, the overall output state is approximately in a tensor product form of all frequency contributions, which indicates that the entanglement is additive. Thus we define a quantity called the entanglement rate as

$$E_R = \frac{1}{2\pi} \int E_F(\omega) d\omega. \tag{18}$$

Intuitively, E_R tells how efficient a system is in generating entanglement. In Fig. 3(b), we calculate E_R for varied optomechanical cooperativities ($C_{om} = 1, 5, 10$) by scanning the ratio $\mathcal{R} = \kappa_e/4g_{\rm em}$ (fixing $g_{\rm em} = 2\pi \times 2$ MHz) such that the system goes from the strong to the weak coupling regime. First, we see that the entanglement rate goes up and down smoothly and reaches a maximal value when the system is around the exceptional point $\mathcal{R} = 1$. The rate E_R decreases as we further increase or decrease the ratio \mathcal{R} . The reason is that a larger \mathscr{R} means a smaller \mathcal{C}_{em} , leading to further cooperativity mismatch and thus reducing the entanglement rate, while a smaller \mathcal{R} indicates a lower microwave extraction ratio $\kappa_{\rm e,c}/\kappa_{\rm e,i}$, effectively decreasing the entanglement rate. Moreover, comparing different C_{om} values in Fig. 3(b), we find that E_R is larger in general for larger C_{om} before the system becomes unstable, and the peak values of E_R shift to

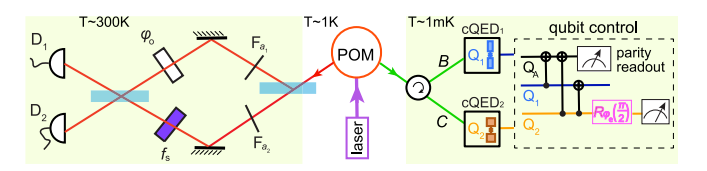


FIG. 4. Schematic setup for detecting M-O Bell pairs encoded in the frequency-bin degree of freedom. The optical photon is analyzed with a balanced Mach-Zehnder interometer, composed of two 50:50 beam splitters (light blue), two narrow-band filters (short black line), a phase shifter (φ_o) , and a frequency shifter (f_s) . Two single-photon detectors are used in the end. Microwave photon detection is realized by cQED systems, where the microwave photon is converted into transmon qubit $(Q_1 \text{ or } Q_2)$ excitation by Raman absorption, followed by a parity measurement, a CNOT operation, a $\pi/2$ rotation along the axis $(\sin \varphi_e, \sin \varphi_e, 0)$, and a high-fidelity single-qubit readout.

the left with an increasing $C_{\rm om}$, which relates to the fact that the approximation $\kappa_{\rm o} \gg g_{\rm om}$ we used is getting worse, such that the exceptional point will shift accordingly.

Throughout the paper, there are several other approximations that merit summarizing here. First, in writing the system Hamiltonian, the rotating wave approximation is used, which is a very good approximation since the blue side band is far from resonant. Second, we require $g_{em} \gg |\kappa_e - \kappa_m| 4$ to ensure that the system is strongly coupled, such that we can approximately define two hybridized modes as in Eq. (10). If the condition is not satisfied, the hybridized modes would in general not be orthogonal, which requires a more complicated description. Third, we also require a weak squeezing such that an approximately Bell state can be obtained with a reasonable fidelity. If the squeezing is too strong, the Bell state fidelity will be reduced as shown in the next section.

V. VERIFYING THE BELL STATE IN THE FREQUENCY-BIN DEGREE OF FREEDOM

Given the output state feature in the strong coupling regime, we propose an experimental scheme for detecting entangled M-O photon pairs encoded in the frequency-bin degree of freedom. As discussed previously, if we decrease the laser pump strength, a standard Bell state in the frequency bin is expected in the ideal case [56]:

$$|\Psi\rangle_{\text{eo}} = \frac{\sqrt{2}}{2} (\hat{a}_1^{\dagger} \hat{B}^{\dagger} + \hat{a}_2^{\dagger} \hat{C}^{\dagger}) |\text{vac}\rangle.$$
 (19)

In practice, considering the existence of dissipation and thermal fluctuation, we could only get the output entangled states with a certain Bell state fidelity. In this section, we discuss such an experimental scheme to verify the entangled state.

A. The experimental scheme for entanglement verification

As shown schematically in Fig. 4, a POM device driven by a blue-detuned laser generates entangled M-O states, whose correlation properties are then detected by the generalized optical and microwave photon detectors shown by the light-green blocks. For a given Bell state, its quantum correlation is revealed by the statistics of measuring each party on a certain chosen basis. For some specific bases, the measurement

results could show a much stronger correlation than predicted by classical physics. In the current scheme, we choose the basis that is defined on the equator of the Bloch sphere for optical and microwave qubits, which can be tuned by changing the phases φ_0 and φ_e .

On the optical side, the optical photon is guided into a balanced Mach-Zehnder interferometer with two 50:50 beam splitters. The first beam splitter separates the photon into two paths: one goes through a filter [57,58] which selects the \hat{a}_1 mode and a phase shifter which shifts the phase φ_0 ; the other goes through a filter selecting the \hat{a}_2 mode and a frequency shifter [59] shifting the mode by frequency $2g_{\rm em}$, such that the two photon modes become indistinguishable. Then the photons interfere at the second beam splitter. A photon click at the single-photon detector D_1 or D_2 projects the optical state on $|\varphi_0\rangle_+ = \frac{\sqrt{2}}{2}(\hat{a}_1^{\dagger} \pm \hat{a}_2^{\dagger}e^{i\varphi_0})|vac\rangle$.

on $|\varphi_{\rm o}\rangle_{\pm} = \frac{\sqrt{2}}{2}(\hat{a}_1^{\dagger} \pm \hat{a}_2^{\dagger} e^{i\varphi_{\rm o}}) |{\rm vac}\rangle$. On the microwave side, the possible state detection is enabled by two circuit quantum electrodynamical (cQED) systems, each consisting of a transmon qubit with matched dispersive coupling to the cavity modes, respectively. In detail, the microwave photon first goes through a circulator, where modes \hat{B} and \hat{C} are guided into two different cQED systems. cQED1 and cQED2 are designed to be resonant only with mode \hat{B} and mode \hat{C} , respectively, such that mode \hat{B} can only be captured by cQED1 and mode \hat{C} only by cQED2. The microwave photons are then converted to qubit excitation with the help of stimulated Raman absorption [60]. This step effectively realizes entanglement swapping from microwave photons to transmon qubits [61]. Immediately after the Raman absorption, a parity measurement is done with the help of an ancillary qubit QA to ensure that one and only one of the two qubits is excited [62]. This heralding operation excludes the zero-photon and higher-order events, increasing the entanglement fidelity significantly. When an odd parity is obtained, we continue to perform a CNOT gate to factor out Q1, then apply a $\pi/2$ rotation on Q₂ along the axis ($\sin \varphi_e$, $\cos \varphi_e$, 0) defined on the Bloch sphere. Finally, a high-fidelity singlequbit readout [63,64] projects qubit Q_2 onto the state $|\varphi_e\rangle_{\pm} =$ $\frac{\sqrt{2}}{2}(|g\rangle \pm |e\rangle e^{-i\varphi_e})$, which is effectively similar to detecting the microwave state $|\varphi_{\rm e}\rangle_{\pm}=\frac{\sqrt{2}}{2}(\hat{B}^{\dagger}\pm\hat{C}^{\dagger}e^{-i\varphi_{\rm e}})\,|{\rm vac}\rangle.$ In summary, the experimental setup allows us to directly

In summary, the experimental setup allows us to directly measure any states on the equator plane defined on the optical and microwave Bloch spheres. Given two fixed phases φ_0 and φ_e , repeated measurements could yield the average value

$$E(\varphi_{o}, \varphi_{e}) = p_{\varphi_{o}, \varphi_{e}}^{+,+} + p_{\varphi_{o}, \varphi_{e}}^{-,-} - p_{\varphi_{o}, \varphi_{e}}^{+,-} - p_{\varphi_{o}, \varphi_{e}}^{-,+}, \tag{20}$$

where each p denotes the probability of coincident counting clicks for the corresponding state projections, e.g., $p_{\varphi_0,\varphi_e}^{+,+} = p(|\varphi_0\rangle_+, |\varphi_e\rangle_+)$. Each probability can be theoretically calculated and the details are reported in the Appendix.

B. CHSH inequality violation and Bell state fidelity lower bound

The Bell inequality provides a strong manifestation for entanglement, whose violation excludes the possibility of all local hidden variable theories. We use the CHSH-type Bell inequality (|S| < 2), which can be tested in our proposed experimental setup by measuring the correlation [65]

$$S = E(\varphi_0, \varphi_e) + E(\varphi'_0, \varphi'_e) + E(\varphi'_0, \varphi_e) - E(\varphi_0, \varphi'_e). \quad (21)$$

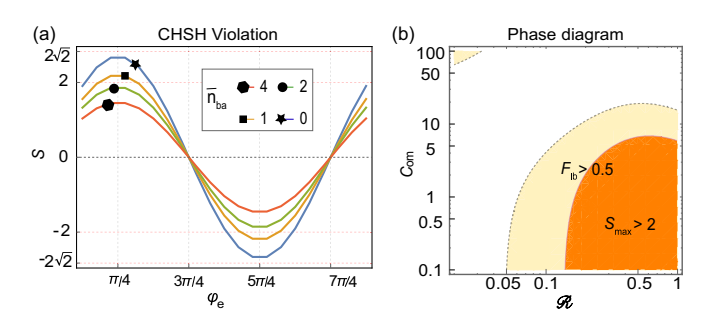


FIG. 5. (a) S correlation curves in terms of the phase angle $\phi_{\rm e}$ with varied thermal baths, taking $\mathscr{R}=\kappa_{\rm e}/4g_{\rm em}=0.26$ and $\mathcal{C}_{\rm om}=1$. (b) "Phase diagram" for a CHSH inequality violation and a Bell-state fidelity larger than 1/2 in the strong coupling regime with $\mathscr{R}<1$. $\bar{n}_{\rm ba}=1$.

In Fig. 5(a), we simulate the typical correlation curve by fixing $\varphi_o = 0$ and varying the phase φ_e (choosing $\varphi_o' = \varphi_o + \pi/2$, $\varphi_e' = \varphi_e + \pi/2$). First, a clear Bell inequality violation is observed |S| > 2 for low thermal noise, indicating the existence of strict entanglement. Also, the violation becomes less obvious as we increase the thermal excitation and the threshold is about two thermal photons. In Fig. 5(b), we map out the parameter regime (orange region) that violates the Bell inequality. We see that this regime does not overlap the regime where E_F is maximal, because the regime with the maximized E_F is around the system's unstable area, where extremely mixed entangled states are generated that could be unsuitable for Bell testing using the proposed experimental setup.

Less demanding evidence of entanglement is given by a Bell state fidelity, which physically measures the closeness between a given state and a standard Bell state. A fidelity larger than 1/2 indicates entanglement. In experiments, a quantity easier to measure is the lower bound of the fidelity, which is given by

$$F_{lb} = \frac{1}{2} \left(p_{0,0}^{+,+} + p_{0,0}^{-,-} + p_{\frac{\pi}{2},\frac{\pi}{2}}^{+,+} + p_{\frac{\pi}{2},\frac{\pi}{2}}^{-,-} - p_{\frac{\pi}{2},\frac{\pi}{2}}^{-,+} - 2\sqrt{p_{0,0}^{+,-} p_{0,0}^{-,+}} \right).$$
(22)

In Fig. 5(b), we also delineate the parameter regime where the fidelity's lower bound is larger than 1/2 (light-yellow region). As expected, this regime is much broader than that of CHSH violation since an entangled state is not necessarily Bell nonlocal. Because it is easier to measure, the lower bound of the fidelity could be a first experiment in M-O entangled photon pair verifications.

VI. M-O STATE CORRELATION FUNCTION AND COINCIDENCE COUNTING RATE

For the transduction scheme to work, we want the entangled photon generation rate to be as large as possible. Thus it is necessary to estimate the coincidence counting rate, including possible transmission losses and detector dark counts. This can be done by exploring the second-order correlation

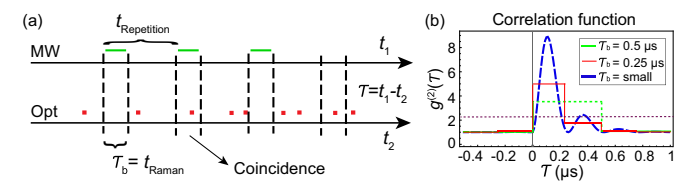


FIG. 6. (a) Schematic of the M-O photon coincidence counting measurement. The microwave measurement repetition time is several microseconds, which includes the qubit preparation, operation, and Raman absorption time, which sets the detection time window τ_b . (b) Second-order correlation function for three detection time resolutions, shown by the long-dashed blue, solid red, and short-dashed green lines. For these lines, we have $\mathcal{C}_{om}=1$, $\kappa_{e,c}/\kappa_{e,i}=20$, and $\bar{n}_{ba}=1$. The dashed horizontal line is determined by $2+\xi_0+\xi_0+\xi_0+\xi_0$.

function [66]

$$g^{(2)}(\tau) = \frac{\langle \hat{a}_{\text{out,c}}^{\dagger}(t+\tau)\hat{c}_{\text{out,c}}^{\dagger}(t)\hat{c}_{\text{out,c}}(t)\hat{a}_{\text{out,c}}(t+\tau)\rangle}{\langle \hat{a}_{\text{out,c}}^{\dagger}(t+\tau)\hat{a}_{\text{out,c}}(t+\tau)\rangle \langle \hat{c}_{\text{out,c}}^{\dagger}(t)\hat{c}_{\text{out,c}}(t)\rangle}, \quad (23)$$

where τ denotes the time delay between the optical and the microwave photon detection. Using the quantum moment-factoring theorem [67], we rewrite the function as

$$g^{(2)}(\tau) = 1 + \frac{R_{\text{oe}}(\tau)R_{\text{eo}}(\tau)}{R_{\text{o}}R_{\text{e}}},$$
 (24)

where $R_{\rm o}$ and $R_{\rm e}$ are the optical and microwave photon generation rates.

$$R_{\rm o} = \langle \hat{a}_{\rm out,c}^{\dagger}(t) \hat{a}_{\rm out,c}(t) \rangle = \frac{1}{2\pi} \int \langle \hat{a}_{\rm out,c}^{\dagger}(-\omega) \hat{a}_{\rm out,c}(-\omega) \rangle d\omega,$$

$$R_{\rm e} = \langle \hat{c}_{\rm out,c}^{\dagger}(t) \hat{c}_{\rm out,c}(t) \rangle = \frac{1}{2\pi} \int \langle \hat{c}_{\rm out,c}^{\dagger}(\omega) \hat{c}_{\rm out,c}(\omega) \rangle d\omega.$$
(25)

 $R_{\text{oe}}(\tau)$ and $R_{\text{eo}}(\tau)$ are called the M-O correlation rates:

$$R_{\text{oe}}(\tau) = \langle \hat{a}_{\text{out,c}}^{\dagger}(t+\tau)\hat{c}_{\text{out,c}}^{\dagger}(t) \rangle$$

$$= \frac{1}{2\pi} \int \langle \hat{a}_{\text{out,c}}^{\dagger}(-\omega)\hat{c}_{\text{out,c}}^{\dagger}(\omega) \rangle e^{-i\omega\tau} d\omega,$$

$$R_{\text{eo}}(\tau) = \langle \hat{c}_{\text{out,c}}(t)\hat{a}_{\text{out,c}}(t+\tau) \rangle$$

$$= \frac{1}{2\pi} \int \langle \hat{c}_{\text{out,c}}(\omega)\hat{a}_{\text{out,c}}(-\omega) \rangle e^{i\omega\tau} d\omega. \tag{26}$$

Equation (24) assumes an infinite time resolution of the photon detector. However, as shown in Fig. 6(a), the photon detector in practice can only resolve photons in a finite time window τ_b . For the optical detector, the time resolution is generally within a nanosecond. However, in microwave detection, the Raman absorption is of the order of a microsecond, within which the arrival time of the microwave photon cannot be distinguished, and it sets the length of the detection time window. Due to this finite time resolution, the measured second-order correlation function is generally a piecewise function,

$$g^{(2)}(\tau_i) = 1 + \frac{\int_{\tau_i}^{\tau_i + \tau_b} R_{\text{oe}}(\tau) R_{\text{eo}}(\tau) d\tau}{R_{\text{o}} R_{\text{e}} \tau_b},$$
 (27)

TABLE II. Feasible parameters of the photon transmission coefficients, detector dark count rates, and detector efficiencies.

$\overline{\eta_{ m o}}$	$\eta_{ m e}$	D_{o}	D_{e}	$T_{ m e}$	$T_{\rm o}$
0.8	0.9	~20 Hz	$\sim 10^3 \text{ Hz}$	0.5	10^{-3}

in which $\tau_{i+1} = \tau_i + \tau_b$. With this formula, we plot the $g^{(2)}(\tau)$ functions with varied detection resolutions in Fig. 6(b). The blue curve represents the ideal case where the detector has an infinite time resolution. First, we see an oscillation structure with a period of around 0.25 μ s, which is due to frequency beating in the strong coupling regime, and it matches exactly the mode splitting $2g_{\rm em} = 2\pi \times 4$ MHz. Second, $g^{(2)}(\tau)$ is not symmetric and the maximal value does not occur with a zero time delay. The reason is that the optical and microwave photons have different time profiles, thus their convolution generally is asymmetric.

Equation (27) can be rewritten as

$$g^{(2)}(\tau_i) := \frac{R_{\rm cc}(\tau_i)}{R_{\rm ac}} = \frac{R_{\rm o}R_{\rm e}\tau_{\rm b} + \int_{\tau_i}^{\tau_i + \tau_{\rm b}} R_{\rm oe}(\tau)R_{\rm eo}(\tau)d\tau}{R_{\rm o}R_{\rm e}\tau_{\rm b}},$$
(28)

where the numerator defines the coincidence counting rate, and we see that it contains two parts: the first is the accidental coincidence rate $R_{\rm ac}=R_{\rm o}R_{\rm e}\tau_b$, while we call the second the correlated coincidence rate. With the parameters in Table I and taking $\tau_{\rm b}=0.5~\mu{\rm s}$, $C_{\rm om}=1$, $\mathcal{R}=0.26$, $\bar{n}_{\rm ba}=1$, we find that the coincidence counting rate is of the order of $R_{\rm cc}\sim10^4$ Hz.

In practice, the experiment also suffers from photon transmission loss and detector dark counts and inefficiencies. To give a general model, we denote $T_{\rm o}$ and $T_{\rm e}$ the optical and microwave transmission coefficients, $D_{\rm o}$ and $D_{\rm e}$ the optical and microwave detector dark count rates, and $\eta_{\rm o}$ and $\eta_{\rm e}$ the optical and microwave detector efficiencies, respectively. Taking into account all of these influences and requiring the correlated coincidence rate to be much larger than the accidental coincidence rate, a simple inequality can be obtained,

$$g^{(2)}(\tau_i) > 2 + \xi_0 + \xi_e + \xi_0 \xi_e,$$
 (29)

which acts as a useful criterion for ensuring successful entanglement verification. The quantities $\xi_{\rm o}=\frac{D_{\rm o}}{\eta_{\rm o}T_{\rm o}R_{\rm o}}$ and $\xi_{\rm e}=$ $\frac{D_{\rm e}}{\eta_{\rm e}T_{\rm e}R_{\rm e}}$, which obviously represent the ratio of dark count rate to photon detection rate. The smaller ξ_0 and ξ_e are, the better the performance of the experiment will be. With the feasible parameters listed in Table II, the coincidence counting rate is reduced to the order of 10 Hz. Also, we show the quantity 2 + $\xi_{\rm o} + \xi_{\rm e} + \xi_{\rm o} \xi_{\rm e} \simeq 2.37$, which is depicted by the dashed purple line in Fig. 6(b). We see that the inequality, Eq. (29), can indeed be satisfied as long as the photon detectors have good enough time resolutions. It is noteworthy that the numerical evaluation is based on current state-of-the-art technological parameters [39]. Given the fast development in this field, we anticipate that the correlated coincidence rate will become even better. In summary, when designing experiments, all these factors, together with the transmission coefficients and detector efficiencies, must be optimized simultaneously, and the theoretical framework given above provides a useful guide for experimentally manifesting M-O entanglement.

VII. DISCUSSION

The entanglement generated from generic electrooptomechanics can also be investigated in the time-bin degree of freedom, where two short pump pulses with a fixed time separation should be applied [31]. In comparison, this time-bin encoding is suitable for a weakly coupled system, while a strongly coupled system is convenient for encoding the frequency-bin entanglement due to the frequency separation of the two hybridized modes. Although we can also study frequency-bin entanglement with a weakly coupled system, it generally involves multiple frequency-separated mechanical and microwave modes in the beginning, which complicates the experimental design. Also, frequency-bin encoding uses a continuous laser drive, which is simpler to implement compared to the time-separated pulse pump and the time delay operation in time-bin encoding (it generally places a demanding requirement for phase stability control in experiments).

Demonstrating M-O entanglement is the first and most important step in DT. Once an entangled source with a high fidelity can be provided, we can adopt the well-developed teleportation scheme [68,69] for quantum transductions. More broadly, M-O entanglement can also be used to directly entangle distant microwave nodes by adopting the well-known DLCZ scheme [70]. As mentioned in the beginning, ET is compatible with the state-of-the-art technological development, and thus, its experimental implementation is much less demanding. The discussion in this paper thus provides a timely guide for pursuing this direction.

ACKNOWLEDGMENTS

We acknowledge support from the ARL-CDQI (W911NF-15-2-0067, W911NF-18-2-0237), ARO (W911NF-18-1-0020, W911NF-18-1-0212), ARO MURI (W911NF-16-1-0349), AFOSR MURI (FA9550-14-1-0052, FA9550-15-1-0015), DOE (DE-SC0019406), NSF (EFMA-1640959), and Packard Foundation. This work was performed, in part, at the Center for Nanoscale Materials, a U.S. Department of Energy Office of Science User Facility, and supported by the U.S. Department of Energy, Office of Science, under Contract No. DE-AC02-06CH11357.

APPENDIX: COINCIDENCE COUNTING PROBABILITY

For given output M-O modes with frequency ω , the coincidence counting probability can be theoretically calculated by modeling the optical and microwave detection as an on-off photon detector, which is described by a set of positive operator-valued measurements [71],

$$\hat{\Pi}_{\text{off}} = \sum_{n=0}^{\infty} (1 - \eta)^n |n\rangle \langle n|, \qquad (A1)$$

$$\hat{\Pi}_{on} = \mathbf{I} - \hat{\Pi}_{off},\tag{A2}$$

in which $|n\rangle$ is the photon number state of the mode being detected and η models the detector efficiency. Thus, the joint probability is given by $P_{\rm on}^{\rm o,e}(\omega)={\rm tr}(\hat{\rho}\hat{\Pi}_{\rm on}^{\rm o}(\omega)\otimes\hat{\Pi}_{\rm on}^{\rm e}(\omega))$, where $\hat{\rho}$ is the M-O output state density matrix. Since we are dealing with Gaussian states, it is convenient to express $\hat{\rho}$ as the Wigner function,

$$W(\mathbf{x}) = \frac{\exp\left(-\frac{1}{2}\mathbf{x}^T\mathbf{V}^{-1}\mathbf{x}\right)}{(2\pi)^2\sqrt{\det\mathbf{V}}},$$
 (A3)

where $V=V_{\text{oe}}^{\text{out}}(\omega)$ is the corresponding covariance matrix. The coincidence counting probability can be evaluated by

$$P_{\text{on}}^{\text{o,e}}(\omega) = \int W(\mathbf{x}) \tilde{\Pi}_{\text{on}}^{\text{o,e}}(\mathbf{x}) d\mathbf{x}. \tag{A4}$$

 $\tilde{\Pi}_{on}^{o,e}(\mathbf{x})$ is the Weyl transform of $\hat{\Pi}_{on}^{o} \otimes \hat{\Pi}_{on}^{e}$ defined by

$$\tilde{\Pi}_{\text{on}}^{\text{o,e}}(\mathbf{x}) = \int \left\langle \mathbf{q} + \frac{\mathbf{q}'}{2} \middle| \hat{\Pi}_{\text{on}}^{\text{o}} \otimes \hat{\Pi}_{\text{on}}^{\text{e}} \middle| \mathbf{q} - \frac{\mathbf{q}'}{2} \middle| e^{i\mathbf{p}^{\mathsf{T}}\mathbf{q}'} d\mathbf{q}', \quad (A5)$$

where we denote $(\mathbf{q}, \mathbf{p}) = (x_0, x_e, p_0, p_e)$. With this formula and taking into account the beam splitter and phase shifter in the experiment, we obtain

$$P_{\varphi_{o},\varphi_{e}}^{+,+}(\omega) = 1 - \frac{2}{(2 - \eta_{o})\sqrt{\det \Sigma_{a}}} - \frac{2}{(2 - \eta_{e})\sqrt{\det \Sigma_{c}}} + \frac{4}{(2 - \eta_{o})(2 - \eta_{e})\sqrt{\det \Sigma_{ac}}}$$
(A6)

for detecting the states $|\varphi_{\rm o}\rangle_+$ and $|\varphi_{\rm e}\rangle_+$ simultaneously. The parameters $\eta_{\rm o}$ and $\eta_{\rm e}$ are the generalized optical and microwave detector efficiencies and

$$\Sigma_u = \frac{\eta_o}{2 - \eta_o} \mathbf{V}_u + \mathbf{I}_2,\tag{A7}$$

$$\Sigma_{v} = \frac{\eta_{e}}{2 - n_{e}} \mathbf{V}_{v} + \mathbf{I}_{2}, \tag{A8}$$

$$\mathbf{\Sigma}_w = \mathbf{V} \cdot \left(\frac{\eta_o}{2 - \eta_o} \mathbf{I}_2 \oplus \frac{\eta_e}{2 - \eta_e} \mathbf{I}_2 \right) + \mathbf{I}_4.$$
 (A9)

Further, the total joint detection rate can be obtained by integrating all frequency contributions,

$$P_{\varphi_0,\varphi_e}^{+,+} = \int_{\omega_1}^{\omega_2} P_{\varphi_0,\varphi_e}^{+,+}(\omega) d\omega.$$
 (A10)

The detection rate for other state projections can be derived similarly. In the text, we use the normalized probability

$$p_{\varphi_{0},\varphi_{e}}^{+,+} = \frac{P_{\varphi_{0},\varphi_{e}}^{+,+}}{P_{\varphi_{0},\varphi_{e}}^{+,+} + P_{\varphi_{0},\varphi_{e}}^{-,-} + P_{\varphi_{0},\varphi_{e}}^{+,-} + P_{\varphi_{0},\varphi_{e}}^{-,+}},$$
(A11)

which corresponds to the physical procedure of postselecting coincidence counting events based on the heralding signals.

- J. I. Cirac, P. Zoller, H. J. Kimble, and H. Mabuchi, Phys. Rev. Lett. 78, 3221 (1997).
- [2] H. J. Kimble, Nature 453, 1023 (2008).
- [3] L. Jiang, J. M. Taylor, A. S. Sørensen, and M. D. Lukin, Phys. Rev. A 76, 062323 (2007).
- [4] C. Monroe, R. Raussendorf, A. Ruthven, K. R. Brown, P. Maunz, L.-M. Duan, and J. Kim, Phys. Rev. A 89, 022317 (2014).
- [5] D. N. Matsukevich and A. Kuzmich, Science 306, 663 (2004).
- [6] B. B. Blinov, D. L. Moehring, L.-M. Duan, and C. Monroe, Nature 428, 153 (2004).
- [7] E. Togan, Y. Chu, A. S. Trifonov, L. Jiang, J. Maze, L. Childress, M. V. G. Dutt, A. S. Sørensen, P. R. Hemmer, A. S. Zibrov, and M. D. Lukin, Nature 466, 730 (2010).
- [8] W. F. Koehl, B. B. Buckley, F. J. Heremans, G. Calusine, and D. D. Awschalom, Nature 479, 84 (2011).
- [9] W. B. Gao, P. Fallahi, E. Togan, J. Miguel-Sanchez, and A. Imamoglu, Nature 491, 426 (2012).
- [10] K. De Greve, L. Yu, P. L. McMahon, J. S. Pelc, C. M. Natarajan, N. Y. Kim, E. Abe, S. Maier, C. Schneider, M. Kamp, S. Höfling, R. H. Hadfield, A. Forchel, M. M. Fejer, and Y. Yamamoto, Nature 491, 421 (2012).
- [11] C. Li and P. Cappellaro, arXiv:1904.01556.
- [12] M. Hafezi, Z. Kim, S. L. Rolston, L. A. Orozco, B. L. Lev, and J. M. Taylor, Phys. Rev. A 85, 020302(R) (2012).
- [13] B. T. Gard, K. Jacobs, R. McDermott, and M. Saffman, Phys. Rev. A 96, 013833 (2017).
- [14] R. Hisatomi, A. Osada, Y. Tabuchi, T. Ishikawa, A. Noguchi, R. Yamazaki, K. Usami, and Y. Nakamura, Phys. Rev. B 93, 174427 (2016).

- [15] M. Tsang, Phys. Rev. A 81, 063837 (2010).
- [16] C. Javerzac-Galy, K. Plekhanov, N. R. Bernier, L. D. Toth, A. K. Feofanov, and T. J. Kippenberg, Phys. Rev. A 94, 053815 (2016)
- [17] L. Fan, C.-L. Zou, R. Cheng, X. Guo, X. Han, Z. Gong, S. Wang, and H. X. Tang, Sci. Adv. 4, eaar4994 (2018).
- [18] L. A. Williamson, Y.-H. Chen, and J. J. Longdell, Phys. Rev. Lett. 113, 203601 (2014).
- [19] C. O'Brien, N. Lauk, S. Blum, G. Morigi, and M. Fleischhauer, Phys. Rev. Lett. 113, 063603 (2014).
- [20] R. W. Andrews, R. W. Peterson, T. P. Purdy, K. Cicak, R. W. Simmonds, C. A. Regal, and K. W. Lehnert, Nat. Phys. 10, 321 (2014).
- [21] C. A. Regal and K. W. Lehnert, J. Phys.: Conf. Ser. 264, 012025 (2011).
- [22] J. Bochmann, A. Vainsencher, D. D. Awschalom, and A. N. Cleland, Nat. Phys. 9, 712 (2013).
- [23] J. M. Taylor, A. S. Sørensen, C. M. Marcus, and E. S. Polzik, Phys. Rev. Lett. 107, 273601 (2011).
- [24] S. Barzanjeh, D. Vitali, P. Tombesi, and G. J. Milburn, Phys. Rev. A 84, 042342 (2011).
- [25] Y.-D. Wang and A. A. Clerk, Phys. Rev. Lett. 108, 153603 (2012).
- [26] L. Tian and H. Wang, Phys. Rev. A 82, 053806 (2010).
- [27] L. Midolo, A. Schliesser, and A. Fiore, Nat. Nanotech. 13, 11 (2018).
- [28] T. Bagci, A. Simonsen, S. Schmid, L. G. Villanueva, E. Zeuthen, J. Appel, J. M. Taylor, A. Sørensen, K. Usami, A. Schliesser, and E. S. Polzik, Nature 507, 81 (2014).

- [29] M. Winger, T. D. Blasius, T. P. M. Alegre, A. H. Safavi-Naeini, S. Meenehan, J. Cohen, S. Stobbe, and O. Painter, Opt. Express 19, 24905 (2011).
- [30] A. Pitanti, J. M. Fink, A. H. Safavi-Naeini, J. T. Hill, C. U. Lei, A. Tredicucci, and O. Painter, Opt. Express 23, 3196 (2015).
- [31] C. Zhong, Z. Wang, C. Zou, M. Zhang, X. Han, W. Fu, M. Xu, S. Shankar, M. H. Devoret, H. X. Tang, and L. Jiang, Phys. Rev. Lett. 124, 010511 (2020).
- [32] S. Barzanjeh, M. Abdi, G. J. Milburn, P. Tombesi, and D. Vitali, Phys. Rev. Lett. 109, 130503 (2012).
- [33] A. Rueda, W. Hease, S. Barzanjeh, and J. M. Fink, npj Quantum Info. 5, 1 (2019).
- [34] A. A. Rakhubovsky, N. Vostrosablin, and R. Filip, Phys. Rev. A 93, 033813 (2016).
- [35] M. Zhang, C.-L. Zou, and L. Jiang, Phys. Rev. Lett. 120, 020502 (2018).
- [36] H.-K. Lau and A. A. Clerk, npj Quantum Info. 5, 31 (2019).
- [37] A. P. Higginbotham, P. S. Burns, M. D. Urmey, R. W. Peterson, N. S. Kampel, B. M. Brubaker, G. Smith, K. W. Lehnert, and C. A. Regal, Nat. Phys. 14, 1038 (2018).
- [38] A. Vainsencher, K. J. Satzinger, G. A. Peairs, and A. N. Cleland, Appl. Phys. Lett. 109, 033107 (2016).
- [39] X. Han, C. Xiong, K. Y. Fong, X. Zhang, and H. X. Tang, New J. Phys. 16, 063060 (2014).
- [40] M. Xu, X. Han, C.-L. Zou, W. Fu, Y. Xu, C. Zhong, L. Jiang, and H. X. Tang, Phys. Rev. Lett. 124, 033602 (2020).
- [41] C.-L. Zou, X. Han, L. Jiang, and H. X. Tang, Phys. Rev. A 94, 013812 (2016).
- [42] N. Moiseyev, Non-Hermitian Quantum Mechanics (Cambridge University Press, Cambridge, UK, 2011).
- [43] X. Han, W. Fu, C. Zhong, C.-L. Zou, Y. Xu, A. A. Sayem, M. Xu, S. Wang, R. Cheng, L. Jiang et al., arXiv:2001.09483.
- [44] A. A. Clerk, M. H. Devoret, S. M. Girvin, F. Marquardt, and R. J. Schoelkopf, Rev. Mod. Phys. 82, 1155 (2010).
- [45] C. Weedbrook, S. Pirandola, R. García-Patrón, N. J. Cerf, T. C. Ralph, J. H. Shapiro, and S. Lloyd, Rev. Mod. Phys. 84, 621 (2012).
- [46] M. A. De Gosson, Symplectic Geometry and Quantum Mechanics, Vol. 166 (Springer Science & Business Media, Berlin, 2006).
- [47] In general, the hybridized modes is not orthogonal to each other due to matrix **M**'s being non-Hermitian.
- [48] C. M. Bender and S. Boettcher, Phys. Rev. Lett. 80, 5243 (1998).
- [49] W. Chen, Ş. K. Özdemir, G. Zhao, J. Wiersig, and L. Yang, Nature 548, 192 (2017).

- [50] P. Marian and T. A. Marian, Phys. Rev. Lett. 101, 220403 (2008).
- [51] S. Tserkis and T. C. Ralph, Phys. Rev. A 96, 062338 (2017).
- [52] A single output frequency corresponds to the use of a filter with an infinitely small bandwidth.
- [53] E. X. DeJesus and C. Kaufman, Phys. Rev. A 35, 5288 (1987).
- [54] Y.-D. Wang, S. Chesi, and A. A. Clerk, Phys. Rev. A 91, 013807 (2015).
- [55] L. Tian, Phys. Rev. Lett. 110, 233602 (2013).
- [56] Strictly, the \hat{a}_1 , \hat{a}_2 , \hat{B} , and \hat{C} mode operators here should represent the output modes. We have omitted the subscript "out" for simplicity.
- [57] The filter should have a bandwidth of several megahertz. This extremely narrow-band filter has been demonstrated with rare-earth ion-doped crystals.
- [58] S. E. Beavan, E. A. Goldschmidt, and M. J. Sellars, J. Opt. Soc. Am. B 30, 1173 (2013).
- [59] X. Guo, Y. Mei, and S. Du, Optica 4, 388 (2017).
- [60] P. Campagne-Ibarcq, E. Zalys-Geller, A. Narla, S. Shankar, P. Reinhold, L. Burkhart, C. Axline, W. Pfaff, L. Frunzio, R. J. Schoelkopf, and M. H. Devoret, Phys. Rev. Lett. 120, 200501 (2018).
- [61] The swap realizes $|1\rangle_B |g\rangle_{Q_1} \rightarrow |0\rangle_B |e\rangle_{Q_1}$ and $|1\rangle_C |g\rangle_{Q_2} \rightarrow |0\rangle_C |e\rangle_{Q_2}$, which gives an entangled state between optical photons and the transmon qubits $\frac{\sqrt{2}}{2}(|1\rangle_{a_1} |e\rangle_{Q_1} + |1\rangle_{a_2} |e\rangle_{Q_2})$.
- [62] M. A. Nielsen and I. Chuang, *Quantum Computation and Quantum Information* (AAPT, 2002).
- [63] S. Shankar, M. Hatridge, Z. Leghtas, K. M. Sliwa, A. Narla, U. Vool, S. M. Girvin, L. Frunzio, M. Mirrahimi, and M. H. Devoret, Nature 504, 419 (2013).
- [64] M. Hatridge, S. Shankar, M. Mirrahimi, F. Schackert, K. Geerlings, T. Brecht, K. M. Sliwa, B. Abdo, L. Frunzio, S. M. Girvin, R. J. Schoelkopf, and M. H. Devoret, Science 339, 178 (2013).
- [65] J. F. Clauser, M. A. Horne, A. Shimony, and R. A. Holt, Phys. Rev. Lett. 23, 880 (1969).
- [66] R. J. Glauber, Phys. Rev. 130, 2529 (1963); 131, 2766 (1963).
- [67] J. H. Shapiro and K.-X. Sun, JOSA B 11, 1130 (1994).
- [68] C. H. Bennett, G. Brassard, C. Crépeau, R. Jozsa, A. Peres, and W. K. Wootters, Phys. Rev. Lett. 70, 1895 (1993).
- [69] D. Bouwmeester, J.-W. Pan, K. Mattle, M. Eibl, H. Weinfurter, and A. Zeilinger, Nature **390**, 575 (1997).
- [70] L.-M. Duan, M. D. Lukin, J. I. Cirac, and P. Zoller, Nature 414, 413 (2001).
- [71] A. Ferraro, S. Olivares, and M. G. Paris, arXiv:quantph/0503237.